Intermetallics 173 (2024) 108427

Contents lists available at ScienceDirect

Intermetallics

journal homepage: www.elsevier.com/locate/intermet

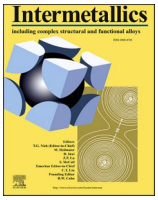

The staggered dual-phase structure in $AlCoCrFeNi_{2.1}$ eutectic high-entropy alloys for superior irradiation and corrosion resistance

Zhou Yang [a], Feida Chen [a,b,*], Shangkun Shen [c], Kun Yang [a,b], Daniu Han [a], Yuanfei Li [d], Chenxin Lu [a,d], Yanwei Zhang [d], Xiaobin Tang [a,b,**]

[a] Department of Nuclear Science & Technology, Nanjing University of Aeronautics and Astronautics, Nanjing, 211106, China
[b] Key Laboratory of Nuclear Technology Application and Radiation Protection in Astronautics, Ministry of Industry and Information Technology, Nanjing, 211106, China
[c] State Key Laboratory of Nuclear Physics and Technology, Department of Technical Physics, School of Physics, Peking University, Beijing, 100871, China
[d] Suzhou Nuclear Power Research Institute, Suzhou, 215004, China

ARTICLE INFO

Keywords:
Eutectic high-entropy alloys
Heterointerfaces
Cold-rolling
Irradiation resistance
Corrosion resistance

ABSTRACT

The cold-rolling process yields a staggered dual-phase structure in the $AlCoCrFeNi_{2.1}$ eutectic high-entropy alloy (EHEA), showcasing resilience against high-temperature and high-pressure water corrosion in the rigorous radiation environment of nuclear reactors. This novel alloy not only fosters heterointerfaces to promote the self-healing of radiation defects but also strategically exploits the variation in corrosion resistance between the FCC and B2 phases to construct barriers hindering the diffusion of corrosion. In contrast to traditional $AlCoCrFeNi_{2.1}$ EHEAs, where corrosion behaviors under radiation predominantly stem from the FCC phase, exacerbating the overall corrosion, our experiments demonstrate that the augmented anti-radiation performance of the FCC phase in the staggered dual-phase structure of $AlCoCrFeNi_{2.1}$ EHEAs significantly mitigates the impact of coupled irradiation and corrosion effects. This study elevates the performance of $AlCoCrFeNi_{2.1}$ EHEAs to a higher echelon, offering fresh insights into the role of heterointerfaces in EHEAs.

1. Introduction

High-entropy alloys (HEAs) have garnered increasing attention over the past decades due to their distinctive properties, including excellent strength [1–3], high ductility [4–6], and radiation tolerance [7,8]. These attributes make HEAs widely applicable in aerospace, automotive industries, and nuclear reactors. Recent developments indicate that eutectic HEAs (EHEAs), featuring both FCC and BCC microstructures, successfully address the strength-ductility trade-offs observed in single-phase HEAs. This leads to a significant enhancement of mechanical properties across a wide temperature range [9–11]. Notably, $AlCoCrFeNi_{2.1}$ EHEAs have attracted considerable interest owing to their remarkable toughness (exceeding 20 % ductility with a tensile strength of 1100 MPa) since their initial report in 2014 [12]. Extensive research indicates that the outstanding mechanical properties of $AlCoCrFeNi_{2.1}$ EHEAs stem from synergistic effects involving various strengthening mechanisms, such as substitutional solid solution strengthening [13], phase boundaries strengthening [14], and nanoprecipitates strengthening [15]. This synergistic strengthening approach offers novel insights into microstructure design strategies. Applying phase-selective recrystallization to $AlCoCrFeNi_{2.1}$ EHEAs, based on this theory, achieves a fine-grain dual-phase microstructure, enabling the fracture strength of EHEAs to reach 1850 MPa while retaining high ductility at 30 % [16].

Despite these notable mechanical properties, ensuring service security is imperative for the application of new materials in extreme working conditions within nuclear reactors. While HEAs, due to their chemical disorder and the addition of passivation-assisted elements, exhibit comparable or superior anti-corrosion performance compared to traditional stainless steels and low-carbon steels, the dual-phase structure of EHEAs results in different corrosion rates between phases. Existing research, such as that conducted by Duan et al. [17] and Song et al. [18], demonstrated varying passivation behaviors of FCC and B2 phases on $AlCoCrFeNi_{2.1}$ EHEAs in different solutions. Additionally, the unique lamellar structure of $AlCoCrFeNi_{2.1}$ EHEAs raises the risk of localized corrosion under pressure water reactor (PWR) coolant

* Corresponding author. Department of Nuclear Science & Technology, Nanjing University of Aeronautics and Astronautics, Nanjing, 211106, China.
** Corresponding author. Department of Nuclear Science & Technology, Nanjing University of Aeronautics and Astronautics, Nanjing, 211106, China.
E-mail addresses: fdchen@nuaa.edu.cn (F. Chen), tangxiaobin@nuaa.edu.cn (X. Tang).

https://doi.org/10.1016/j.intermet.2024.108427
Received 24 April 2024; Received in revised form 24 June 2024; Accepted 10 July 2024

environments, where phase boundaries may act as preferentially corroded sites, forming micro-galvanic corrosion between phases. As of now, our understanding of the localized corrosion behavior and mechanism of $AlCoCrFeNi_{2.1}$ EHEAs remains limited.

Furthermore, the intense neutron irradiation within nuclear reactors affects the segregation of elements, the evolution of phase and grain boundaries, and the redistribution of nanoprecipitates, thereby promoting corrosion of EHEAs under PWR coolant environments. Given that cold-rolling strengthens $AlCoCrFeNi_{2.1}$ EHEAs through the synergistic effects of various hetero-structures, they may exhibit heightened sensitivity to neutron irradiation compared to other HEAs. However, these heterointerface structures are also expected to influence the behavior of radiation defects, potentially mitigating radiation damage caused by neutron irradiation [17–19]. Currently, the scientific community studying radiation damage in materials has shown significant interest in alloys with heterointerface structures. Therefore, exploring the degradation behavior and passivation enhancement of $AlCoCrFeNi_{2.1}$ EHEAs under irradiation is of paramount importance, both for advancing the nuclear reactor's application of $AlCoCrFeNi_{2.1}$ EHEAs and gaining a better understanding of the role of heterointerface structures during irradiation.

In this study, we achieved the construction of staggered dual-phase structures on $AlCoCrFeNi_{2.1}$ EHEAs through cumulative cold-rolling and annealing processes. The radiation influence on different phases and heterointerface structures involving phase boundaries, grain boundaries, and nanoprecipitates was thoroughly discussed. High-density phase and grain boundaries in alloys demonstrated remarkable stability under irradiation, not only suppressing radiation defects in the nearby area but also acting as barriers to impede the diffusion of defects between different phases. Simultaneously, the staggered dual-phase structures significantly suppressed the diffusion of corrosion, resulting in enhanced irradiation and corrosion resistance in $AlCoCrFeNi_{2.1}$ EHEAs. This work expands our understanding of the role of heterointerfaces in the radiation effects on EHEAs.

2. Materials and methods

$AlCoCrFeNi_{2.1}$ EHEAs were melted in a vacuum suspension melting furnace using pure raw materials of 99.9 %. The ingots underwent three rounds of inversion and remelting to ensure the homogeneity of alloy composition. The composition of dual-phase in the as-cast alloys is shown in Table 1 by EDS. The resulting as-cast specimens, measuring 20 mm × 25 mm × 4 mm, underwent cumulative cold-rolling to attain a final thickness of 0.6 mm. Subsequently, the specimens were annealed at a rate of 5 °C/min to 660 °C for 1 h, followed by cooling in air to eliminate residual stresses generated during material preparation. Both the as-cast and staggered dual-phase structure specimens were cut into dimensions of 6 mm × 6 mm × 0.6 mm and polished before use. The samples were etched by a mixed solution of 0.5 mg $FeCl_3$, 1 ml 45 wt% HCl and 9 ml ultrapure water to observe the microstructure of the alloys by SEM.

An irradiation experiment employing 6 MeV Au^{3+} was conducted on the 2 × 1.7 MeV tandem accelerator at Peking University, reaching a fluence of 2.1 × 10^{16} cm^{-2} at room temperature to study equivalent radiation effects caused by neutrons. According to SRIM calculations, the peak damage of the alloy reached 24 dpa at a depth of approximately 450 nm in Fig. 1. The specimens were placed in a corrosion cell, immersed in a solution containing 1000 ppm B, 10 ppm Cl, and 2 ppm Li

Table 1
The composition of dual-phase in the as-cast alloys.

	Al (at%)	Co (at%)	Cr (at%)	Fe (at%)	Ni (at%)
FCC	2.46	23.27	23.76	23.17	27.34
B2	27.28	9.24	2.83	7.81	52.84
theoretical	16.39	16.39	16.39	16.39	34.43

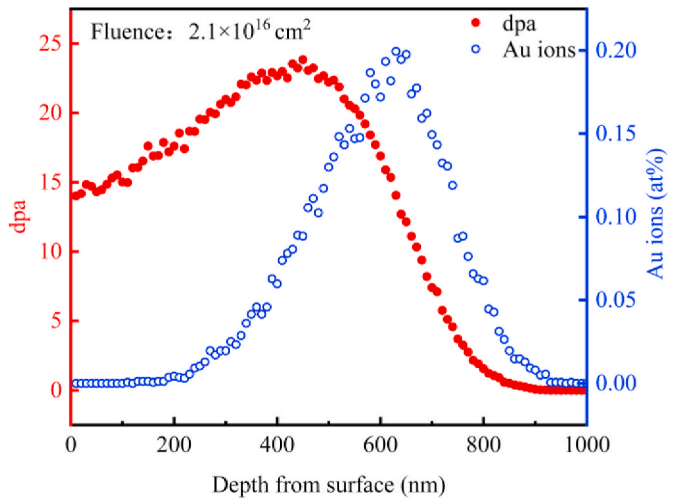

Fig. 1. Irradiation damage distribution of 6 MeV Au^{3+} ions in $AlCoCrFeNi_{2.1}$ EHEAs using SRIM simulation.

at 320 °C and 13 MPa, simulating the operating water chemistry and temperature conditions in pressurized water reactors (PWRs). The solution was deaerated to less than 200 ppb O, and the corrosion duration was 165 h. Microstructures of $AlCoCrFeNi_{2.1}$ EHEAs were observed using SEM and TEM. The focused ion beam (FIB) lift-out technique was employed to prepare the specimens on an FEI Helios G4 UX, and measurements were conducted using an FEI Tecnai G2 F20 S-TWIN transmission electron microscope.

3. Results and discussion

In Fig. 2 (a), the XRD spectra of as-cast and cold-rolled $AlCoCrFeNi_{2.1}$ EHEAs samples are essentially consistent, with clear peaks observed for both FCC and B2 phases. The preferred orientation of the FCC (111) plan observed in the as-cast sample is disrupted by the cold-rolling process. Fig. 2(d) and (e) show the low magnification micrographs of microstructures of the as-cast sample and the cold-rolling sample by SEM. Fig. 2(f) displays the typical lamellar structure of the as-cast $AlCoCrFeNi_{2.1}$ EHEAs. As shown in Fig. 2(g), this regular lamellar structure transforms into randomly distributed equiaxial crystals, each in approximately 200 ± 98.9 nm scale. This gives rise to a staggered dual-phase structure characterized by phase boundaries and grain boundaries arranged in a crisscross pattern following cold-rolling and annealing treatment. Although the hardness of FCC and B2 phases differed substantially, the grain size of each phase shows no significant difference. The lattice constants were derived from the diffraction patterns and the XRD, and the lattice constants of the as-cast alloy were 3.59 Å for the FCC phase and 2.87 Å for the B2 phase, while those of the cold-rolled alloy were 3.59 Å for the FCC phase and 2.87 Å for the B2 phase. The lattice constants in the table indicate that annealing at 660 °C for 1 h effectively released the residual stresses introduced by cold-rolling. The orientation relationship between FCC and B2 phases after cold-rolling and annealing can be expressed as $(11\text{-}1)_{FCC}\|(101)_{B2}$, $<011>_{FCC}\|<\text{-}111>_{B2}$, as obtained from Fourier image analysis in Fig. 2(j). The phase boundaries are not entirely coherent. A large number of edge dislocations formed in the 2–5 nm width nearby region of the phase boundaries, alternately constituted by the densely packed faces of dual-phase (Fig. 2 (j)). The formation of dislocations arrays may due to the hindering effect of interfaces on dislocations and the mutual squeezing that occurs during the growth process of dual-phase [20]. Besides the K–S relationship of $(11\text{-}1)_{FCC}\|(101)_{B2}$, $<011>_{FCC}\|<\text{-}111>_{B2}$, other orientation relationship like $(01\text{-}1)_{B2}\|(33\text{-}2)_{FCC}$ and $(321)_{B2}\|(112)_{FCC}$ was also reported in the previous studies [20], but we didn't observe in this work. In the SAED images of Fig. 2(f), there are discernible additional diffraction

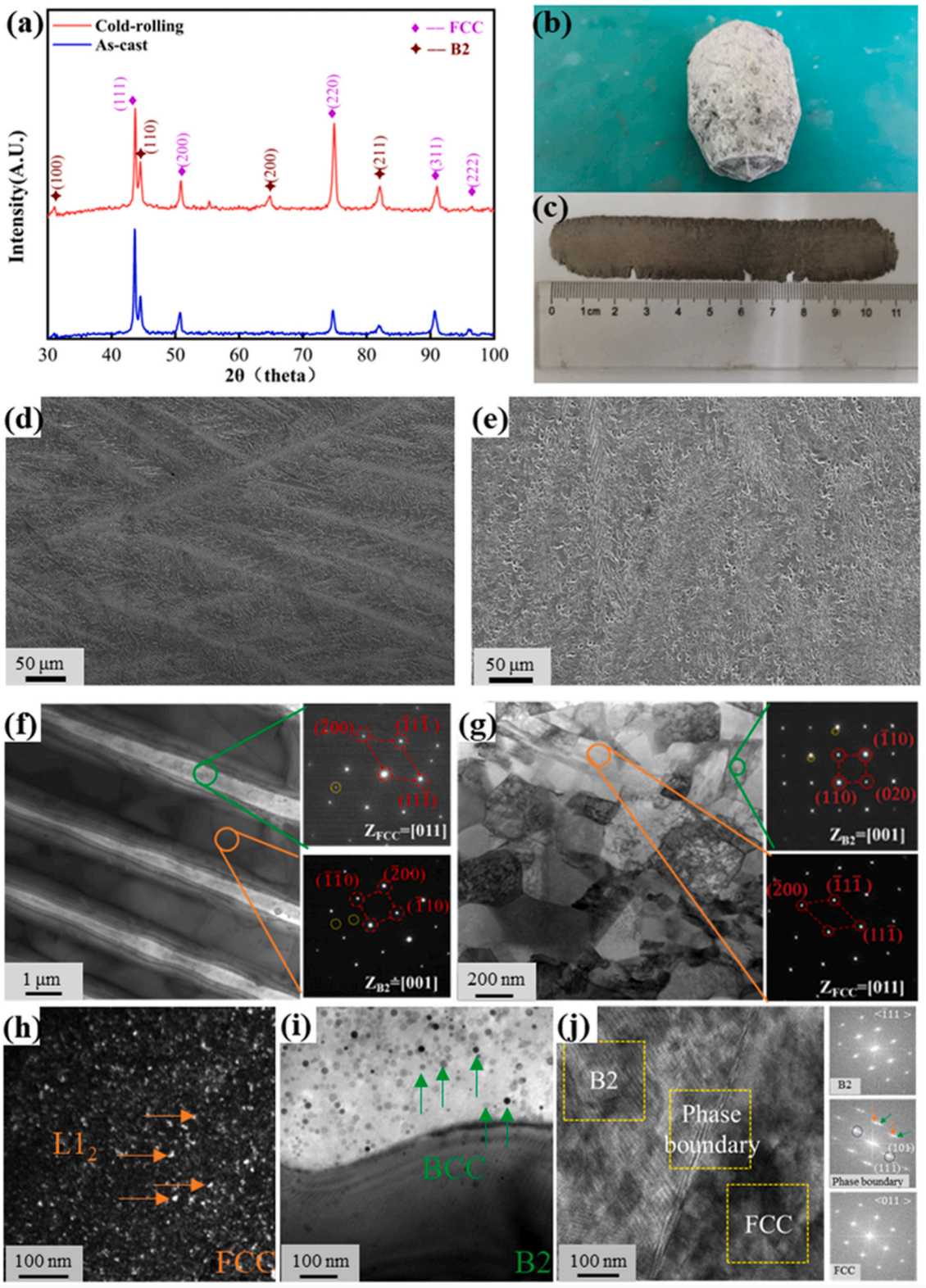

Fig. 2. Microstructure of the as-cast and the cold-rolling $AlCoCrFeNi_{2.1}$ EHEAs. (a) XRD images of two types $AlCoCrFeNi_{2.1}$, (b) the ingot of the as-cast alloy; (c) cold-rolling sample, (d) SEM images of the as-cast sample, (e) SEM of the cold-rolling sample, (f) TEM images and SAED of the as-cast sample at the corresponding positions, (g) TEM images and SAED of the cold-rolling the corresponding positions; (h) TEM image of $L1_2$ nano precipitations in the FCC phase of the as-cast sample, (i) TEM image of BCC nano precipitations in B2 phases of the as-cast sample; (j) HRTEM image and Fourier diagram of phase boundary.

spots encircled by yellow circles, implying the presence of distinct phase structures within the dual-phase of the alloy. However, the additional diffraction pattern is incomplete making it difficult to ascertain the precise structure of these other phases. Moreover, as illustrated in Fig. 2 (h) and (i), an abundance of nanoparticles is evident within both the FCC and B2 phases in the as-cast alloys. Previous research [21,22] indicates that the nanoparticles observed within the FCC phase correspond to the Al- and Ni-rich $L1_2$ phases, while those within the B2 phase align with the Cr-rich BCC phase. The formation of BCC nano-precipitations in B2 phase due to the spinodal decomposition phenomenon [23], while the formation of Ni–Al enriched $L1_2$ nano-precipitations in FCC phase can be attributed to the strongly negative mixing enthalpy of the Ni–Al pair [24]. However, the $L1_2$ phase nano-precipitation in the FCC phase disappeared after cold-rolling and annealing.

The microstructure of the as-cast and the staggered dual-phase $AlCoCrFeNi_{2.1}$ EHEAs after Au ion irradiation is depicted in Figs. 3 and 4. Fig. 3(a) shows a clear irradiation-induced defect band at a depth of 1.5 μm from the surface in the as-cast EHEAs. However, while intense irradiation inevitably introduces defects into alloys, irradiation-induced defect bands were not observed in the staggered dual-phase $AlCoCrFeNi_{2.1}$ EHEAs in this study. Both phase boundaries and grain boundaries exhibit notable stability, with no observable amorphization and element segregation even under a 24 dpa radiation damage dose (Figs. 3 and 4).

Based on the TEM images of the irradiated as-cast alloy (Fig. 3), further observation of radiation defects in staggered dual-phase $AlCoCrFeNi_{2.1}$ EHEAs was performed at a similar depth range. As shown in Fig. 5(a–c), there are some black points observed within the grains of the FCC phase, which could potentially be attributed to either irradiation defects or nanoprecipitation. In this work, the black points are irradiation defects for reasons that will be discussed in detail next. Additionally, it is noteworthy that no irradiation defects have been detected within the grains of the B2 phase.

Similar to the as-cast $AlCoCrFeNi_{2.1}$ EHEAs, the survived radiation dislocation loops formed in FCC and B2 phases in staggered dual-phase $AlCoCrFeNi_{2.1}$ EHEAs exhibit distinct properties. As shown in Fig. 3, the average size of the radiation dislocation loops formed in the FCC phase is roughly 7 nm, considerably larger than the size in the B2 phase (~3 nm) after 24 dpa Au ion irradiation. The loop density in the FCC phase (3.7×10^{21} m^{-3}) is higher than that in the B2 phase (2.8×10^{21} m^{-3}). In staggered dual-phase $AlCoCrFeNi_{2.1}$ EHEAs, discrepancies between FCC and B2 phases persist. As shown in Fig. 5(a)-5(d), radiation dislocation loops are observed within the FCC phase grains, while no loops present in the B2 phase. In the present study, the B2 phase exhibits higher irradiation tolerance than the FCC phase in both the as-cast and the staggered dual-phase EHEAs. This phenomenon is due to the differences in the composition and structure of the dual phases. In previous reports [25–27], it has been generally observed that BCC-phase alloys have a higher defect formation energy than FCC-phase alloys. Consequently, BCC-phase alloys have demonstrated better irradiation tolerance than FCC-phase alloys. Additionally, the average size of dislocation loops (~3.5 nm) in the FCC phase of staggered dual-phase $AlCoCrFeNi_{2.1}$ EHEAs is smaller than that in the as-cast alloy (~7 nm), while the density (4.9×10^{21} m^{-3}) is higher than that in the as-cast alloys (3.7×10^{21} m^{-3}). The increased grain boundaries and phase boundaries serve to absorb irradiated defects to hinder the aggregation [28,29] and diffusion of irradiation defects in the dual-phases, resulting in the better irradiation resistance of staggered dual-phase EHEAs than the as-cast EHEAs.

Fig. 6 shows the EDS images of the variations in nanoprecipitations of the as-cast and the staggered dual-phase $AlCoCrFeNi_{2.1}$ EHEAs before and after Au ion irradiation. The size of BCC precipitation in the B2 phase of staggered dual-phase $AlCoCrFeNi_{2.1}$ EHEAs coarsens to 18.2 ± 6.6 nm after cold-rolling and annealing, with a reduced number density

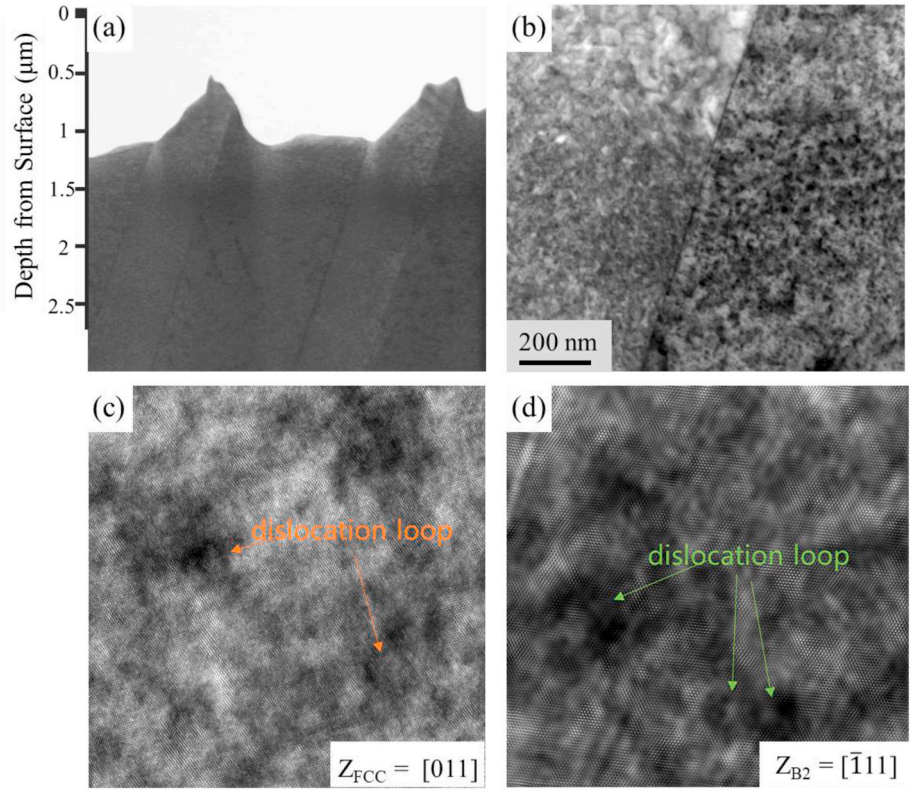

Fig. 3. Internal damage morphology and phase boundary microstructure of irradiated as-cast alloy. (a) STEM bright field image of irradiated defects along the depth distribution of the as-cast alloy; (b) STEM bright field image of the damage peak region; (c) HRTEM image at the peak region of the FCC phase; (d) HRTEM map at the peak region of the B2 phase.

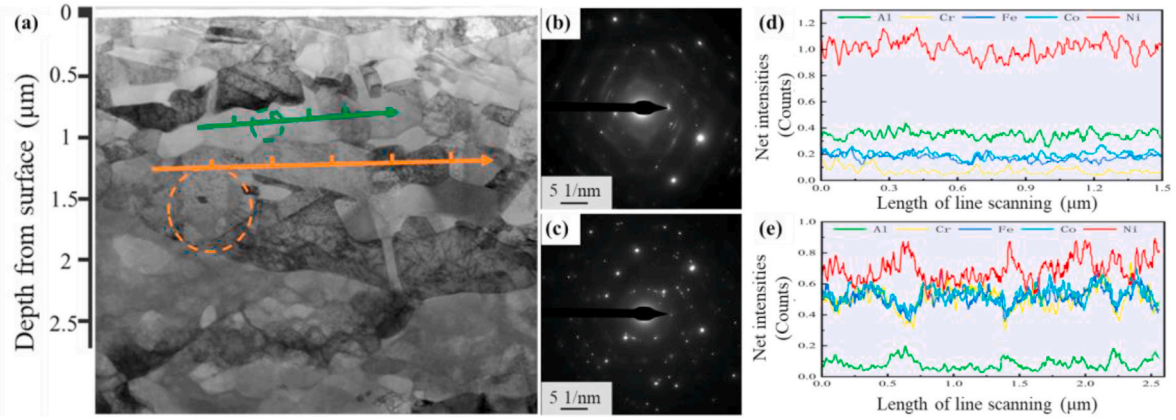

Fig. 4. Irradiation damage morphology of cold-rolling alloy. (a) the irradiation defects STEM bright-field image of the cold-rolling alloy along the depth distribution; (b) the SAED patterns of the grains inside the irradiated regions of B2 phases (green circle); (c) the SAED patterns of the grains inside the irradiated regions of the FCC phases (orange circle); (d) the line scanning energy spectra of the grains in the inner regions of the irradiated regions of the B2 phases (green line); (e) the line scanning energy spectra of the grains in the inner regions of the irradiated regions of the FCC phases (orange line).

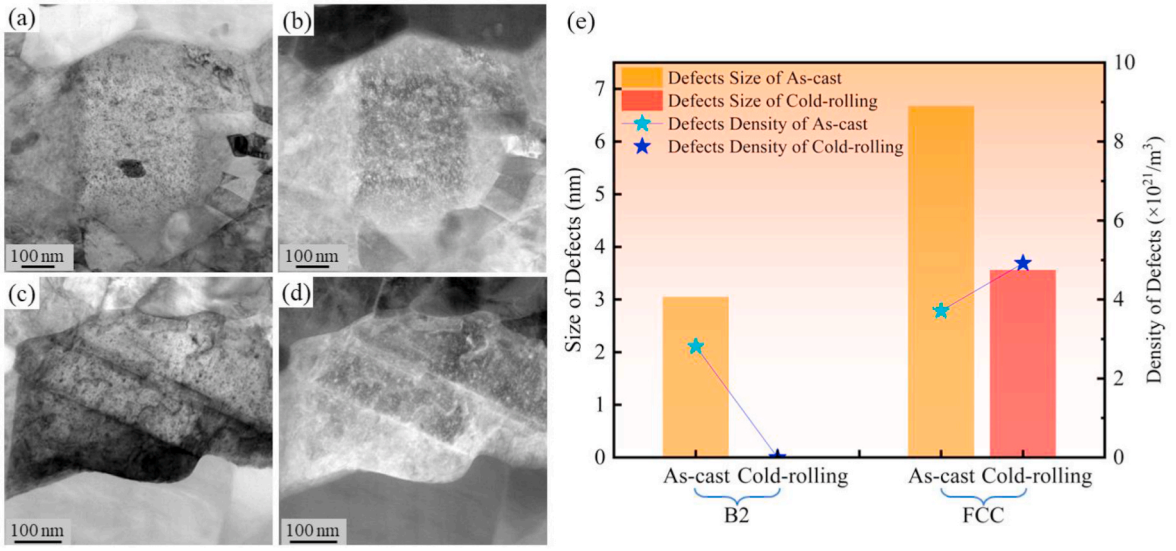

Fig. 5. Morphology and statistics of irradiated defects in the cold-rolling alloy. (a), (c) STEM bright-field images of the internal grain in the irradiated area; (b), (d) STEM dark-field images of (a), (c); (e) statistical diagram of the irradiated defects in the cold-rolling alloy.

of $2.7 \times 10^{21}/m^3$. However, as illustrated in Fig. 6(d3), the size of BCC precipitation dissolves to 11.6 ± 5.9 nm after irradiation. The $L1_2$ phase nano-precipitations, enriched with Al and Ni, which dissolved in the FCC phase after annealing, do not re-form after irradiation. The coarsening of BCC nanoprecipitates and dissolution of $L1_2$ nanoprecipitates observed in this study is consistent with the results reported by Zarei-Hanzaki et al. [30]. Therefore, it can be inferred that all the black points correspond to irradiation defects in Fig. 5. In Fig. 6(b3), the size and number density of the BCC precipitation do not change significantly after irradiation in the case of as-cast samples. The different performance of the $L1_2$ nanoprecipitations and the BCC nanoprecipitations under the Au ions irradiation is due to the disordering of the $L1_2$ nanoprecipitations [31]. The disordering of the $L1_2$ nanoprecipitations is a common and interesting feature of the irradiation response of the FCC phase in $AlCoCrFeNi_{2.1}$ [32,33]. The irradiation induced defects raise the free energy of the matrix and provide the driving force needed for the transformation from the $L1_2$ phase to the FCC phase, resulting in the dissolution of the $L1_2$ nanoprecipitations [34]. However, the dissolution of BCC nanoprecipitations under irradiation in the staggered dual-phase $AlCoCrFeNi_{2.1}$ EHEAs may result from ballistic mixing, which describes the ejection of atoms from nanoprecipitations – and the resultant shrinking of nanoprecipitations – due to ballistic collisions from irradiation damage cascades [35,36]. Additionally, the ballistic mixing provides the means by which Cr is driven to the boundary where it can interact with the matrix [37]. Therefore, the Cr-enriched BCC nanoprecipitations dissolve into the B2 phase of the staggered dual-phase EHEAs and remain stable at approximately 11 nm after irradiation.

As depicted in Fig. 7, B2 phase exhibits worse corrosion resistance than FCC phase in all alloys after immersion in PWR coolant environments for 165 h. Since the FCC phase is enriched with Fe, Cr, and Co, while the B2 phase is enriched with Al and Ni, they are protected by passive films enriched with Cr and Al elements, respectively. The preferential dissolution of the B2 phase is attributed to the more compact Cr_2O_3 composition of the passive film compared to Al_2O_3 (the Pilling-Bedworth ratio is about 1.99 and 1.28 respectively) [17]. Besides, Guo et al. [18] reported the presence of local micro-couples between the FCC and B2 phases of the $AlCoCrFeNi_{2.1}$ EHEA was also a cause of local corrosion. The more active B2 phases function as the anode during corrosion to protect the FCC phase as the local cathode. Therefore, corrosion in the alloy initiate with the formation of micro-galvanic cell

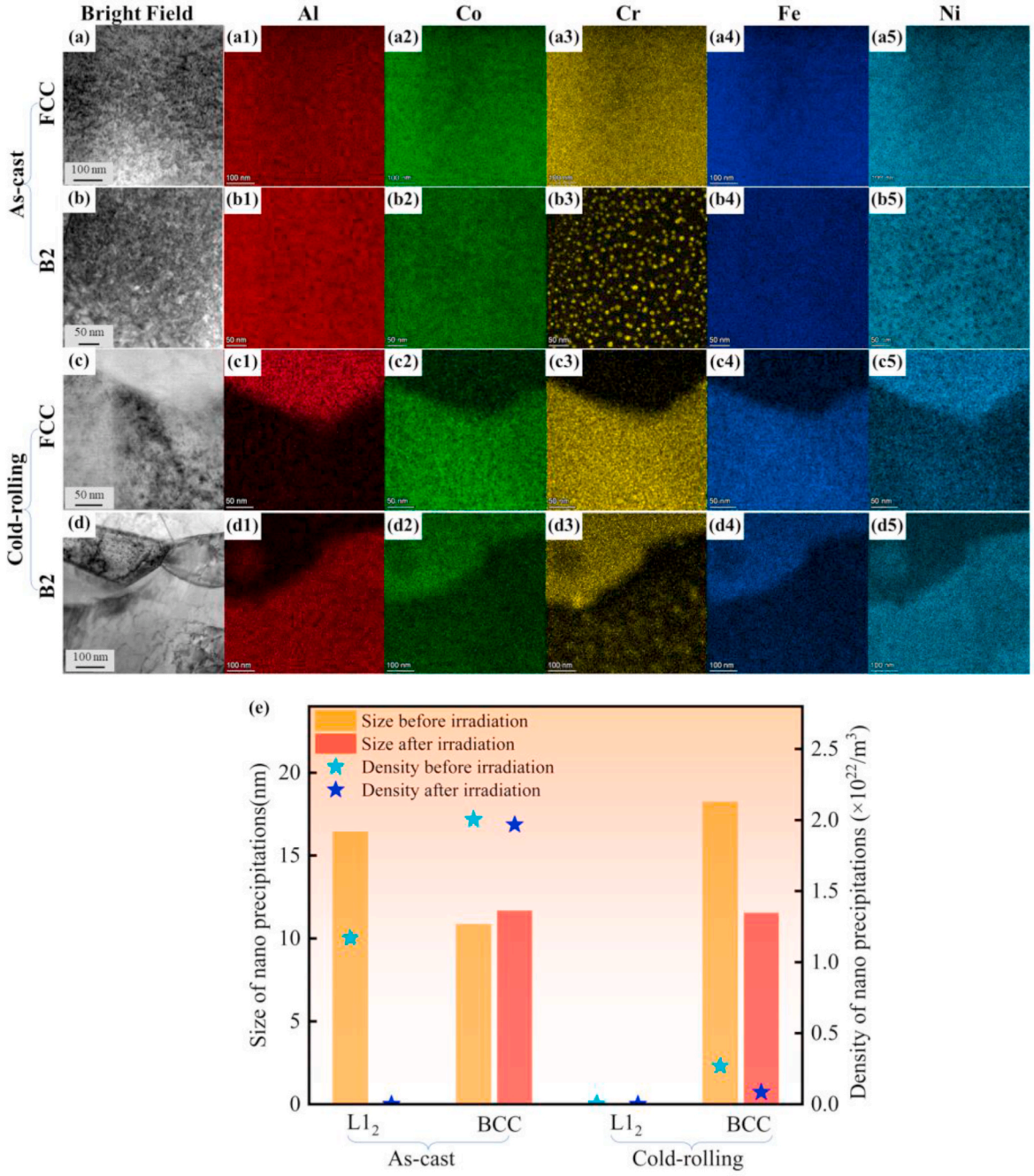

Fig. 6. EDS of the damage regions of two $AlCoCrFeNi_{2.1}$ EHEAs after irradiation and nano precipitations statistics. (ăa5) EDS of the damage peak region of the as-cast FCC phase; (b ~ b5) EDS of the damage peak region of the as-cast B2 phase; (c ~ c5) EDS of the existence of the damage region in the staggered FCC phase; (d ~ d5) EDS near the same depth of the staggered B2 phase; (e) statistical diagram of the nano precipitations in the EHEAs before and after irradiation.

at the microstructural length-scale. At anodic potentials exceeding the breakdown potential, deeper corrosion depth forms in regions of the B2 phases [38]. The above reasons result in the B2 phases have a deeper corrosion depth than the FCC phase.

The increase in grain boundaries in alloys is regarded as detrimental to corrosion resistance [39,40]. As shown in Fig. 7(c), the depth of B2 phase corrosion in some areas of the staggered dual-phase EHEAs has deeper than the as-cast EHEAs, but there are some areas the depth of B2 phase becoming shallower than the as-cast EHEAs due to the phase boundary between B2 phase and FCC phase. This phenomenon shows that although increasing grain boundaries can deepen the corrosion of B2 phase, increasing phase boundaries can hinder the internal diffusion of corrosion in the staggered dual-phase EHEAs. The staggered dual-phase structures of $AlCoCrFeNi_{2.1}$ EHEAs exhibit notably superior corrosion resistance than the as-cast alloys. The regular lamellar structure provides an unimpeded channel for corrosion to occur inner the alloy. In contrast, the randomly distributed eutectic phase boundaries in the staggered dual-phase structures of $AlCoCrFeNi_{2.1}$ EHEAs efficiently prevent the diffusion of oxygen elements due to the better anti-corrosion resistance of FCC phase.

Radiation defects exacerbate alloy corrosion because of the coupled effects of irradiation and corrosion in nuclear reactors. Pre-irradiated samples were employed to study the influence of radiation-corrosion coupled effects on the staggered dual-phase structures of $AlCoCrFeNi_{2.1}$ EHEAs in this study. Since the radiation damage depth reached roughly 2 μm, all corrosion on the pre-irradiated samples occurred in the

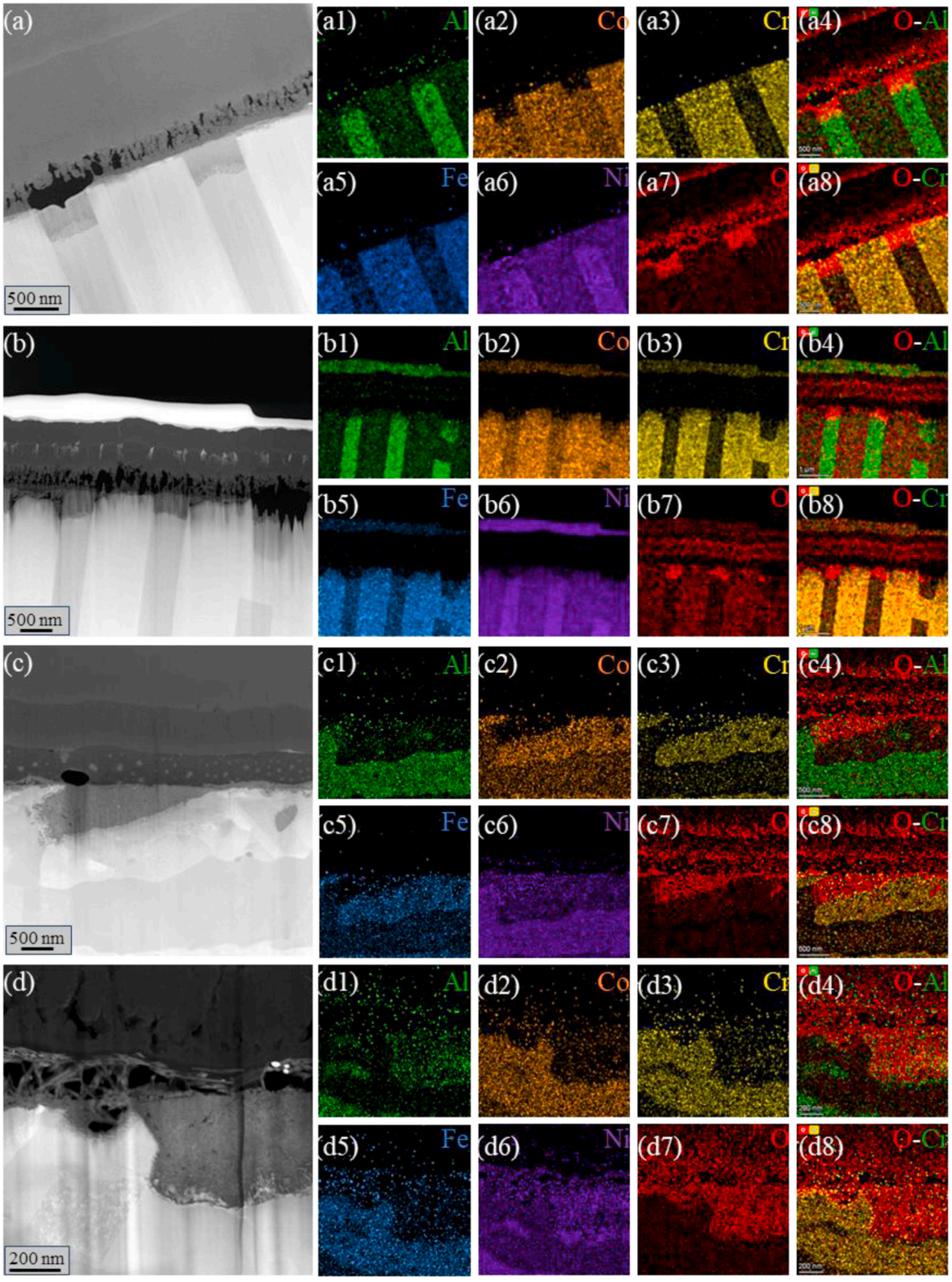

Fig. 7. The cross-section TEM images and EDS mappings of the corroded samples. (a) HADDF image of the corroded as-cast alloy, (a1) -(a8) EDS mappings of the (a); (b) HADDF image of the pre-irradiated as-cast alloy; (b1) -(b8) EDS mappings of the (b); (c) HADDF image of the corroded cold-rolling alloy, (c1) -(c8) EDS mappings of the (c); (d) is HADDF image of the pre-irradiated cold-rolling alloy, (d1) -(d8) EDS mappings of the (d).

radiation-damaged regions, the difference of the corrosion between non-irradiated samples and pre-irradiated samples entirely results from the irradiation defects. By comparing Fig. 7(a) and (b), both the FCC phase and the B2 phase with irradiation defects show a poor corrosion resistance in the as-cast EHEAs, even the boundaries were corroded in the surface. Besides, the O diffused to considerably greater depths in FCC phase than before irradiation. This is due to the worse irradiation resistance and the higher irradiation defects density of the as-cast alloys.

The irradiated-included high point defect concentration could potentially accelerate corrosion due to enhanced diffusion [41]. Experimental data has shown higher diffusion rates along irradiated-included defects in stainless steel [42,43], suggesting that irradiation induced microstructural changes may affect corrosion rates. Therefore, the irradiation accelerates the corrosion of the as-cast EHEAs. Comparing Fig. 7(c) and (d), the corrosion of staggered dual-phase structure $AlCoCrFeNi_{2.1}$ EHEAs with irradiation defects changes little. As discussed earlier, the size and density of irradiation defects in the staggered dual-phase EHEAs in Fig. 7(e) decrease significantly as the grain boundaries and phase boundaries increase. The irradiation accelerated corrosion diffusion decreases due to the improved irradiation resistance in the staggered dual-phase EHEAs. Therefore, the coupled effects of irradiation and corrosion pose reduced risk to the staggered dual-phase structures of $AlCoCrFeNi_{2.1}$ EHEAs than to traditional alloys.

4. Conclusion

In this work, the staggered dual-phase structures of $AlCoCrFeNi_{2.1}$ EHEAs are prepared by the cold-rolling process, and the irradiation and corrosion resistance of the staggered dual-phase $AlCoCrFeNi_{2.1}$ EHEAs. We found that this heterointerface structure exhibits stability even under 24 dpa Au ion irradiation and contributes to the self-healing of radiation defects in the FCC phase. The following conclusions can be drawn:

(1) The B2 phase shows a better irradiation resistance than FCC phase, since the difference of phase structures and the strong chemical bonding between Al and Ni in ordered B2 phase. Besides, the staggered dual-phase structures increase the grain boundaries and phase boundaries absorb irradiated defects to hinder the aggregation and diffusion of irradiation defects. Thus, the staggered dual-phase $AlCoCrFeNi_{2.1}$ EHEAs shows a better irradiation resistance.
(2) The FCC phase shows a better corrosion resistance than B2 phase, since oxides of Cr is more stable than oxides of Al and the presence of local micro-couples between the FCC and B2 phases. Compared with the as-cast alloys, the phase boundaries increased by the staggered dual-phase structures prevent the corrosion diffusion due to the better anti-corrosion resistance of FCC phase.
(3) The staggered dual-phase $AlCoCrFeNi_{2.1}$ EHEAs achieve remarkable irradiation and corrosion resistance through the construction of a distinctive heterointerface structure, and this work provides deeper insights into the role of heterointerfaces in the radiation effects on EHEAs.

CRediT authorship contribution statement

Zhou Yang: Writing – review & editing, Writing – original draft, Supervision, Project administration, Methodology, Investigation, Data curation. **Feida Chen:** Writing – review & editing, Methodology, Investigation, Conceptualization. **Shangkun Shen:** Project administration. **Kun Yang:** Methodology. **Daniu Han:** Formal analysis. **Yuanfei Li:** Project administration. **Chenxin Lu:** Project administration. **Yanwei Zhang:** Project administration. **Xiaobin Tang:** Investigation, Funding acquisition, Formal analysis.

Declaration of competing interest

The authors declare that they have no known competing financial interests or personal relationships that could have appeared to influence the work reported in this paper.

Data availability

Data will be made available on request.

Acknowledgements

This work was supported by the Natural Science Foundation of Jiangsu Province (Grant No. BK20231450) and the Fundamental Research Funds for the Central Universities (Grant No. NS2023029).

References

[1] F. Gao, C. Deng, Y. Sun, et al., Lightweight refractory high entropy alloys with excellent specific strength and enhanced malleability by in-situ heterogeneous structure, Mater. Char. 203 (2023) 113127.
[2] S.H. Shim, H. Pouraliakbar, S.I. Hong, Hierarchical structured as-cast $CrFeNiMn_{0.5}Cu_{0.5}$ high entropy alloy with excellent tensile strength/ductility properties, Scripta Mater. 210 (2022) 114473.
[3] C. Zhang, Q. Yu, Y.T. Tang, et al., Strong and ductile FeNiCoAl-based high-entropy alloys for cryogenic to elevated temperature multifunctional applications, Acta Mater. 242 (2023) 118449.
[4] S. Qin, M. Yang, P. Jiang, et al., Designing structures with combined gradients of grain size and precipitation in high entropy alloys for simultaneous improvement of strength and ductility, Acta Mater. 230 (2022) 117847.
[5] N. Yao, T. Lu, K. Feng, et al., Ultrastrong and ductile additively manufactured precipitation-hardening medium-entropy alloy at ambient and cryogenic temperatures, Acta Mater. 236 (2022) 118142.
[6] T.J. Jang, Y.N. Lee, Y. Ikeda, et al., Compositive role of refractory element Mo in improving strength and ductility of face-centered-cubic complex concentrated alloys, Acta Mater. 255 (2023) 119030.
[7] N. Kumar, C. Li, K. Leonard, et al., Microstructural stability and mechanical behavior of FeNiMnCr high entropy alloy under ion irradiation, Acta Mater. 113 (2016) 230–244.
[8] M. He, S. Wang, S. Shi, et al., Mechanisms of radiation-induced segregation in CrFeCoNi-based single-phase concentrated solid solution alloys, Acta Mater. 126 (2017) 182–193.
[9] Y. Lu, Y. Dong, H. Jiang, et al., Promising properties and future trend of eutectic high entropy alloys, Scripta Mater. 187 (2020) 202–209.
[10] F. He, Z. Wang, P. Cheng, et al., Designing eutectic high entropy alloys of CoCrFeNiNbx, J. Alloys Compd. 656 (2016) 284–289.
[11] P. Shi, R. Li, Y. Li, et al., Hierarchical crack buffering triples ductility in eutectic herringbone high-entropy alloys, Science 373 (2021) 912–918.
[12] Y. Lu, Y. Dong, S. Guo, et al., A promising new class of high-temperature alloys: eutectic high-entropy alloys, Sci. Rep. 4 (2014) 6200.
[13] P. Li, H. Sun, C. Li, et al., A novel strengthening strategy for diffusion bonded joint of $AlCoCrFeNi_{2.1}$ eutectic high entropy alloy to 304 stainless steel, Trans. Nonferrous Metals Soc. China 33 (2023) 2121–2135.
[14] Y. Gao, F. Ge, Y. Cui, et al., Study on the strengthening mechanism of $AlCoCrFeNi_{2.1}$ eutectic high-entropy alloy, J. Alloys Compd. 968 (2023) 171878.
[15] Q. Cheng, Y. Zhang, X.D. Xu, et al., Mechanistic origin of abnormal annealing-induced hardening in an AlCoCrFeNi2.1 eutectic multi-principal-element alloy, Acta Mater. 252 (2023) 118905.
[16] Q. Wu, F. He, J. Li, et al., Phase-selective recrystallization makes eutectic high-entropy alloys ultra-ductile, Nat. Commun. 13 (1) (2022) 4697.
[17] X. Duan, T. Han, X. Guan, et al., Cooperative effect of Cr and Al elements on passivation enhancement of eutectic high-entropy alloy $AlCoCrFeNi_{2.1}$ with precipitates, J. Mater. Sci. Technol. 136 (2023) 97–108.
[18] L. Song, W. Hu, B. Liao, et al., Corrosion behavior of AlCoCrFeNi2.1 eutectic high-entropy alloy in Cl^--containing solution, J. Alloys Compd. 938 (2023) 168609.
[19] Y. Wang, S. Li, F. Chen, et al., Unique dislocation loops distribution of AlCrFeNiTix eutectic high-entropy alloys under high-temperature ion irradiation, J. Alloys Compd. 958 (2023) 170373.
[20] T. Xiong, W. Yang, S. Zheng, et al., Faceted Kurdjumov-Sachs interface-induced slip continuity in the eutectic high-entropy alloy, AlCoCrFeNi2.1, J. Mater. Sci. Technol. 65 (2021) 216–227.
[21] T. Xiong, S. Zheng, J. Pang, et al., High-strength and high-ductility $AlCoCrFeNi_{2.1}$ eutectic high-entropy alloy achieved via precipitation strengthening in a heterogeneous structure, Scripta Mater. 186 (2020) 336–340.
[22] H. Jiang, Z. Ni, J. Wang, et al., Effect of electric current pulse on microstructure and mechanical properties of $AlCoCrFeNi_{2.1}$ eutectic high entropy alloy, Materials Characterization 201 (2023) 112952.
[23] J. Charkhchian, A. Zarei-Hanzaki, A. Moshiri, et al., Unraveling the formation of L12 nano-precipitates within the FCC-phase in AlCoCrFeNi2.1 eutectic high entropy alloy, Vacuum 221 (2024) 112919.
[24] J. Charkhchian, A. Zarei-Hanzaki, A. Moshiri, et al., Spinodal decomposition of B2-phase and formation of Cr-rich nano-precipitates in AlCoCrFeNi2.1 eutectic high-entropy alloy, Adv. Eng. Mater. 25 (16) (2023) 2300164.
[25] Z. Cheng, J. Sun, X. Gao, et al., Irradiation effects in high-entropy alloys and their applications, J. Alloys Compd. 930 (2023) 166768.
[26] H. Zhang, C. Li, Z. Zhu, et al., Effects of He-ion irradiation on the microstructures and mechanical properties of the novel Co-free VxCrFeMnNiy high-entropy alloys, J. Nucl. Mater. 572 (2022) 154074.
[27] O. El-Atwani, N. Li, M. Li, et al., Outstanding radiation resistance of tungsten-based high-entropy alloys, Sci. Adv. 5 (2019) eaav2002.
[28] W.S. Cunningham, K. Hattar, Y. Zhu, et al., Suppressing irradiation induced grain growth and defect accumulation in nanocrystalline tungsten through grain boundary doping, Acta Mater. 206 (2021) 116629.

[29] P. Mao, J. Cui, Y. Chen, et al., Quantitative investigation on sink strength of nano-grain boundary for irradiation resistance, J. Nucl. Mater. 526 (2019) 151741.
[30] J. Charkhchian, A. Zarei-Hanzaki, T.M. Schwarz, et al., Unleashing the microstructural evolutions during hot deformation of as-cast AlCoCrFeNi2.1 eutectic high entropy alloy, Intermetallics 168 (2024) 108253.
[31] J. Pang, T. Xiong, W. Yang, et al., Atomic scale structure dominated FCC and B2 responses to He ion irradiation in eutectic high-entropy alloy $AlCoCrFeNi_{2.1}$, J. Mater. Sci. Technol. 129 (2022) 87–95.
[32] S.L. Jang, C.C. Shih, C.C. Liu, et al., CMOS quadrature VCOs using the varactor coupling technique, IEEE Microw. Wireless Compon. Lett. 21 (9) (2011) 498–500.
[33] H.C. Liu, T.E. Mitchell, Irradiation induced order-disorder in Ni3Al and NiAl, Acta Metall. 31 (6) (1983) 863–872.
[34] M. Nastasi, J.W. Mayer, Thermodynamics and kinetics of phase transformations induced by ion irradiation, Mater. Sci. Rep. 6 (1) (1991) 1–51.
[35] G. Martin, Phase stability under irradiation: ballistic effects, Phys. Rev. B 30 (1984) 1424–1436.
[36] J.P. Wharry, M.J. Swenson, K.H. Yano, A review of the irradiation evolution of dispersed oxide nanoparticles in the b.c.c. Fe-Cr system: current understanding and future directions, J. Nucl. Mater. 486 (2017) 11–20.
[37] S.S. Raiman, G.S. Was, Accelerated corrosion and oxide dissolution in 316L stainless steel irradiated in situ in high temperature water, J. Nucl. Mater. 493 (2017) 207–218.
[38] V. Hasannaeimi, S. Mukherjee, Galvanic corrosion in a eutectic high entropy alloy, J. Electroanal. Chem. 848 (2019) 113331.
[39] E. David, Kathryn F. Varela, Oliver K. Johnson, et al., Measuring simulated hydrogen diffusion in symmetric tilt nickel grain boundaries and examining the relevance of the Borisov relationship for individual boundary diffusion, Acta Mater. 212 (2021) 116882.
[40] R.K. Gupta, N. Birbilis, The influence of nanocrystalline structure and processing route on corrosion of stainless steel: a review, Corrosion Sci. 92 (2015) 1–15.
[41] S. Lapuerta, N. Moncoffre, H. Jaffrézic, et al., Use of the point defect model to interpret the iron oxidation kinetics under proton irradiation, J. Appl. Phys. 101 (2007) 064905.
[42] S. Lozano-Perez, K. Kruska, I. Iyengar, et al., The role of cold work and applied stress on surface oxidation of 304 stainless steel, Corrosion Sci. 56 (2012) 78–85.
[43] S. Cissé, L. Laffont, B. Tanguy, et al., Effect of surface preparation on the corrosion of austenitic stainless steel 304L in high temperature steam and simulated PWR primary water, Corrosion Sci. 56 (2012) 209–216.